Controls on preservation of organic matter during the Cenomanian Ocean Anoxic Event II (OAE2) and Turonian global sea-level rise: Agadir Basin, Morocco

Controls on preservation of organic matter during the Cenomanian Ocean Anoxic Event II (OAE2) and Turonian global sea-level rise: Agadir Basin, Morocco

Jianpeng Wang[1], Jonathan Redfern[1], Luc G. Bulot[2,1], Kevin G. Taylor[1]

1. North Africa Research Group, Department of Earth and Environmental Sciences, University of Manchester, Manchester, M13 9PL, UK.

2. Laboratoire Géosciences Océan (LGO-UMR6538) CNRS - Université de Brest - Université de Bretagne Sud - Place Nicolas Copernic - 29280 PLOUZANE - France

Abstract

The Ocean Anoxic Event II (OAE2) was a significant global event associated with a positive carbon isotope excursion, occurring from the Late Cenomanian to the Early Turonian (C/T). It has been commonly associated with enhanced organic carbon preservation. Carbon isotopic analysis carried out over the C/T interval in the Agadir Basin, Morocco, integrated with previous biostratigraphic data, allows a refined correlation of the OAE2 interval. Detailed sedimentary facies analysis identifies ten lithofacies that record the transition from shallow marine environments in the Late Cenomanian to relatively deeper conditions in the Early Turonian. The variation in lithofacies can be correlated to relative sea level changes that show a correlation to the global eustatic curve.

The OAE2 interval comprises dark grey mudstones beds that display low total organic carbon (TOC) values. Trace element and facies analysis suggest dilution from high detrital influx, along with oxic water conditions and low productivity. OM-rich black mudstones are identified in post-OAE2 Early Turonian strata. Trace element analysis suggests this increase in organic matter accumulation was related to increased sea surface productivity and oxygen-

depleted bottom water conditions, which facilitated organic matter preservation. Deposition of OM-rich black mudstones is widely reported during the global Early Turonian marine transgression, suggesting the very high sea level was a major control on organic matter generation and preservation.

Key words: OAE2, Organic carbon, Stratigraphy, Depositional Environment, Geochemistry, Morocco

1. Introduction

The Oceanic Anoxic Event II (OAE2), spanning the latest Cenomanian to earliest Turonian, is an interval characterized by globally-enhanced organic matter preservation due to anoxic marine palaeoenvironments (Schlanger and Jenkyns, 1976; Schlanger et al., 1987). It was associated with an extremely warm palaeoclimate and high global sea level (Jenkyns, 2003; Forster et al., 2007; Jenkyns, 2010; Sames et al., 2016; Joo et al., 2020). The event is marked by a globally-correlatable positive $\delta^{13}C$ excursion within carbonate strata, resulting from increased global organic matter burial, which preferentially removed $\delta^{12}C$ from seawater (Arthur et al., 1988; Tsikos et al., 2004). Although this positive $\delta^{13}C$ excursion has been extensively recorded in a full range of marine environments from continental shelf to pelagic marine (Jenkyns et al., 1994; Tsikos et al., 2004; Gale et al., 2005; Keller et al., 2008; Jarvis et al., 2011), anoxic conditions were not pervasive during this interval, especially in shallow marine environments (Gertsch et al., 2010b; El-Sabbagh et al., 2011).

Mudstones and interbedded carbonates were deposited in the Agadir Basin, Morocco, along the Atlantic continental margin during the Late Cenomanian and Early Turonian. This provides an opportunity to characterise the nature of the OAE2 event in a shallow marine environment. Sedimentological, mineralogical and palaeontological studies have previously been undertaken on the Azazoul section of the Agadir Basin, which characterised the response to palaeoclimate and sea level change during the C/T interval (Gertsch et al., 2010b; Jati et al., 2010; Fonseca et al., 2020). However, the limited resolution of biostratigraphic evidence and $\delta^{13}C$ and $\delta^{18}O$ data in these previous studies made it difficult to confidently locate the C/T boundary in this succession. Previous workers did not recognise any organic-rich mudstones during the OAE2 interval, although OM-rich black mudstones were developed after the OAE2 interval during the Early Turonian interval (Gertsch et al., 2010b; Jati et al., 2010).

In this study, we present new data that allows for a more precise definition of the C/T boundary in the Agadir Basin. This is achieved through high-resolution carbon isotope analysis, which is integrated with the biostratigraphy data obtained by planktonic foraminifera analysis by Jati (2010). Furthermore, combined sedimentological and inorganic geochemical (trace and major elements) analysis have allowed us to further refine the palaeoenvironmental interpretation during the C/T interval, leading to a better understanding of the response of this shallow marine setting to the OAE2. Additionally, we performed organic and inorganic geochemical, as well as petrographic analysis, to explore the processes controlling organic matter preservation during the OAE2 and post-OAE2 intervals, thereby determining the dominant influence on quality and distribution of organic-rich mudstone deposition in this basin.

2. Geological setting

The Agadir Basin is part of the Western High Atlas range. With a basement of Precambrian metamorphic rocks (Stets and Wurster, 1982), the basin was filled by Palaeozoic, Mesozoic and Cenozoic marine and continental sediments (Nouidar, 2002). The Hercynian Unconformity marks the base of the Mesozoic section, which is overlain by rifted continental red bed facies that characterise the Triassic succession, capped by basaltic flows associated with the opening of the Atlantic Ocean (Nouidar, 2002; Daoudi et al., 2008). During the Jurassic period, a significant marine transgression occurred, leading to deposition of a thick, shallow marine carbonate platform in the Agadir Basin (Duval-Arnould et al., 2021). Epicontinental paralic and marine sediments filled the Agadir Basin during the Early Cretaceous with in gulf embayment setting (Behrens and Siehl, 1982). The Late Cenomanian-Early Turonian marine transgression led to deposition of another extensive marine carbonate sequence in the Agadir Basin (Gertsch et al., 2010b; Jati et al., 2010).

The Azazoul beach section, located at GPS coordinates 30°33′14.821″N, 9°44′24.997″W, is found approximately 25 km to the northwest of Agadir (Figure 1). The coastal section provides a 100-metre thick cliff exposure that dips at an angle of 10 degrees to the south, spanning the Late Cenomanian to Early Turonian time interval. Lithologies observed in this seciton consists of various rock types, including limestone, marly limestone, marls, oyster beds, mudstones and black shales.

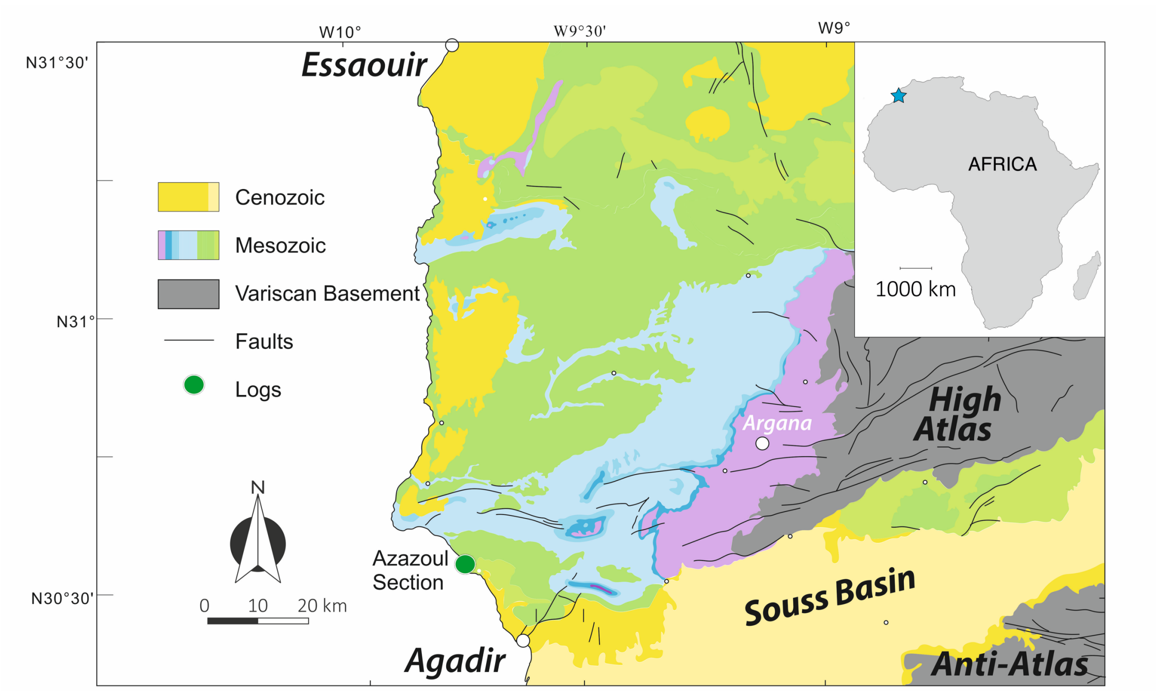

Figure 1 Location of Azazoul section in the Agadir Basin, Morocco. Modified after (Hollard et al., 1985)

3. Database and Methods

During the study of the Late Cenomanian to Early Turonian interval of the Azazoul section, a detailed logging was carried out at a centimetre-scale, and a total of 107 samples were collected for analysis. The samples were systematically analysed in respect to petrography, carbon isotopic stratigraphy, biostratigraphy, mineralogy, organic and inorganic geochemistry.

In total, 69 samples were made into polished thin sections, primarily for lithofacies and biostratigraphy analysis. Total organic and inorganic carbon was measured on chosen 64 samples using a Leco carbon analyser in the University of Manchester and Jilin University , ensuring accurate and consistent results for the carbon content of the samples.

Carbon isotope and oxygen isotope analysis were conducted on all samples at the University of Liverpool using an Elemental Analyser coupled to the Thermo Scientific Delta VAdvantage mass spectrometer, which was fitted with Conflo IV gas handling system. Small amounts of samples, typically a few grams, were carefully selected from the fresh samples collected in the field. Before the isotope analysis, all samples were underwent pre-treatment to remove reactive organic compounds that might present in the bulk limestones. The reported data are present as delta (δ) values with respect to the Vienna Pee Dee Belemnite (VPDB) carbon and oxygen isotope scales (*via* NBS 19, NBS 18). Analytical precision (1σ), based on replicate analysis of in-house quality control calcite, was estimated to be better than ±0.1 ‰ for both carbon and oxygen isotope values.

A set of 37 samples were selected for X-ray fluorescence analysis to obtain trace and major element (TM) data using an Axios Sequential X-ray Fluorescence Spectrometer at the

University of Manchester. To minimize the dilution effects of silica, the trace elements obtained were normalized to aluminium (Turekian and Wedepohl, 1961; Wedepohl, 1971; Brumsack, 1989; Wedepohl, 1995; Morford and Emerson, 1999). All the trace elements are displayed as Al-normalized values with units of 10^{-4}.

Mineralogical quantification was carried out on all the samples using a Philips PW1730 and Bruker D8 Advance at the University of Manchester, to identify the mineral compositions of collected samples.

A total of 64 samples were analysed for Total Organic Carbon content (TOC) from the Azazoul section, using a Lecco carbon analyser from the University of Manchester and Jilin University. Additionally, Rock-Eval measurements were conducted at Jilin University on 17 samples to identify the type and maturity of organic matter and to detect petroleum potential. 100 mg sample was placed in a vessel and progressively heated to 550°C under an inert atmosphere (helium).

4. Results

4.1. Lithofacies and depositional environment

Ten lithofacies were identified in the Azazoul section (Figure 2 and Table 1). These lithofacies were interpreted to record deposition under intertidal to deeper subtidal marine environments. Based on the detailed lithofacies interpretation (Fig 2), skeletal components, mineralogy and sedimentary structures (Table 1, Figs 3 and 4), the depositional environments of the Cenomanian/Turonian strata in the Agadir Basin can be summarised below:

4.1.1. Late Cenomanian, *R. cushmani* zone

The upper part of the *R. cushmani* zone was identified and comprises lithofacies LF1, LF2 and LF3 (Figure 2 and Figure 3). These lithofacies together forms a facies association that records a shallowing-upward sequence, from deep-subtidal to shallow-subtidal facies.

4.1.2. C/T transition, *Whiteinella archaeocretacea* zone

In the studied section, a total of six lithofacies have been identified (Figure 2 and Figure 4). The boundary between the *R. cushmani* and the *W. archaeocretacea* zone is marked as an erosional surface, characterized by a karst surface filled with shell fragments, overlain by a thin layer of grainstone (LF5) (Figure 4 B1). Above the erosional surface, two beds of dark grey clay-rich mudstone (LF4) were developed with a thickness of 0.6m and 0.8m respectively. Between the two mudstone beds is a package of 2.5 m coarse-grained limestone with associated lithofacies LF5, LF6 and LF7. A thick package of oyster beds (LF6) overlies the second mudstone layer. Overlaying the massive oyster beds are fine-grain limestone alternated with grey-dark grey mudstone (LF7) deposition. This is interpreted to record a sea level rise. It is followed by a 2m thick dark grey mudstone (LF1), suggesting deposition in lower energy conditions, probably deeper water settings, and then LF7, which suggests shallowing upward. Thin beds of LF3 sediments dominate the upper part of this zone, capped by an erosional surface filled with bioclastic-rich conglomerate.

The lithofacies association suggests rapid environmental change between high-energy shallow subtidal facies and deep subtidal facies. The upper part is associated with a shallowing-upward succession from a dominantly deep subtidal environment.

4.1.3. Early Turonian, *H. helvetica* zone

The dominant lithofacies identified in the *H. helvetica* zone are yellowish fine-grain limestones and OM-rich black mudstones (Figure 5). The bioclastic conglomerate were overlain a yellowish and reddish limestone-marly limestone (LF8), containing massive calcite nodules. Above this unit, there are several metres of partially laminated calcite-rich black shales with occasional nodules (LF9), followed by a 5m succession of black mudstone beds (LF10), characterised by a large number of large calcite nodules (with diameters up to 50 cm) and cherts (diameter up to 1 m). Towards the top of this zone, the lithofacies shift to dark-grey to black mudstones with fewer nodules (LF9) alternating with some thinly bedded fine-grain limestone layers.

The lithofacies association suggests a short interval of shallowing occurred prior to a significant marine transgression, which led to deposition of relatively thick deep marine sediments. Although there are some occasional shallow-water lithofacies, the *H. helvetica* zone in the Agadir Basin is characterised by dominantly deeper-marine sediments with abundant beds of organic-rich fine-grained mudstone.

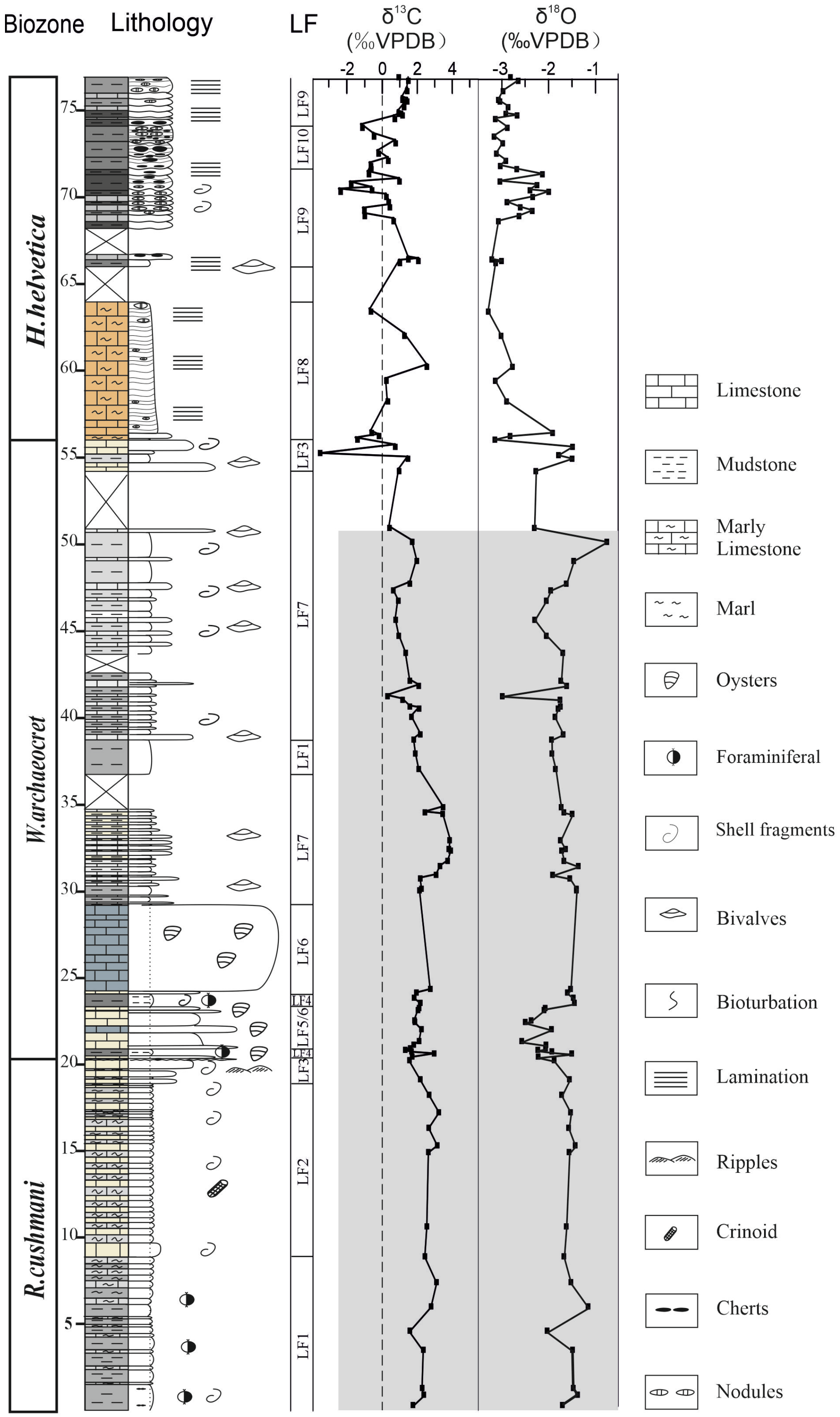

Figure 2 Cenomanian-Turonian succession of the Azazoul Beach in the Agadir Basin, with associated lithofacies, carbon and oxygen isotope curves.

Table 1 Characteristics and interpretation of lithofacies recognised in the C/T succession of the Agadir Basin

Lithofacies	Sedimentological features	Mineralogy	Skeletal composition	Interpretation
LF1: Silt- and clay-bearing, carbonate-rich mudrock	Dark grey mudstone intercalated with some thinly nodular wackestone layers (Figure 3 A1). Presence of erosional surface (Figure 3 A2)	Carbonate dominant (calcite 44.76±15.77%, Ankerite 7.40±5.90%), clay minerals (25.54±11.11%, kaolinite and smectite), quartz (average 13.08±4.68%), albite (average 7.28±3.29%), Muscovite and minor pyrite (<1%).	Oyster and bivalve fragments, and ostracods are locally presented. Planktonic and benthic foraminifera are commonly developed	Subtidal environment, oxic conditions, between the FWWB and SWB
LF2: Shelly wackestone / marly limestone bedding couplet	Thin wackestone beds interbedded with marly limestone beds (Figure 3B1). Individual beds are rarely thicker than 20 cm.	Calcite dominant (81.55±12.21%), ankerite (8.98±4.85%), quartz (5.18±2.64%), clay minerals (2.43±3.06%) and Albite (1.49±1.85%)	Mainly include shell fragments, together with minor foraminifera, gastropods, ostracods fragments (Figure 3 B2)	Subtidal environment, oxic water conditions, between the FWWB and SWB
LF3: Bioturbated, shelly packstone	Alternated with thinly marly limestone beds (Figure 3 C1), and topped by erosional surface (Figure 3 C2)	Calcite dominant (89.56±3.67%), minor ankerite (0.89±1.16%), quartz (6.24±3.10%), minor halite (<1%) and clay minerals (<1%)	Bivalves fragments dominant, and presence of minor gastropods, ostracods, and benthonic foraminifera (Figure 3 C2)	Shallow subtidal environment, above the FWWB
LF4: Silt-bearing, clay rich black mudrocks	Black mudstone, discontinuous planar parallel lamination (Figure 4 A1 and A2). Turbidites with some shelly fragments were recognised	Kaolinite-dominant clay minerals (33.74±4.29%), calcite (16.99±8.17%), quartz (16.92±3.22%), muscovite (12.71±10.08%) albite (10.66±1.86%), and minor pyrite (1.54±1.21%).	Planktonic foraminifera and benthonic foraminifera are both moderately developed, with minor oyster fragments.	Subtidal facies, oxic conditions, between the FWWB and SWB

LF5: Bivalve-rich grainstone/ floatstone	Nodular beds, interbedded with thin marly limestone. Extensively bioturbated (Figure 4 B1)	Calcite dominant (91.08±4.81%), quartz (6.72±3.61%), with minor clay minerals (1.94±2.37%), and very few other minerals.	Composed of shell fragments (oyster dominated), echinoid spines, gastropod, ostracod, benthonic foraminifera (Figure 4 B2)	Shallow subtidal, high energy, oxic conditions, above the FWWB
LF6: Oyster build-up	Massive bedding, composed entirely of shell fragments, bed up to 7 metres thick (Figure 4 B2)	Calcite dominant	Oysters, displaying with different size and shapes, mostly over 10 centimetres in diameter	Intertidal, oxic conditions, above the FWWB
LF7: Grey nodular wackestone	Grey nodular wackestone interbedded with dark grey mudstone, and presence of parallel waves (Figure 4 C1)	Calcite dominant (88.59±13.86%), ankerite (0.90±1.19%), quartz (6.64±11.95%), albite (0.96±1.35%), minor muscovite (1.11±1.27%) clay minerals (0.84±2.34%)	Bivalves fragments and planktonic foraminifera are moderately present, minor benthonic foraminifera (Figure 4 C2)	Subtidal facies, oxic water conditions, between the FWWB and SWB
LF8: Yellowish /reddish wackestone	Fine grain, continuous parallel planar lamination (Figure 5 A1). Cherts and calcite nodules are present	Calcite (87.34±6.68%), ankerite (1.4±3.3%), quartz (10.28±6.11%), minor halite (1.18±0.44%) and muscovite (2.07±1.02%)	Planktonic foraminifera are highly developed (Figure 5 A2) and absence of benthonic foraminifera.	Subtidal, offshore, quite water conditions, below the SWB
LF9: Carbonate rich black mudrock	Partially continuous parallel planar (Figure 5 B1), with some calcite nodules present	Calcite (80.93±7.85%), quartz (14.83±6.46%), muscovite (2.34±1.67%), minor ankerite (0.55±0.76%) and halite (1.00±0.86%)	High planktonic foraminifera content, some radiolarian, rare shell fragments (Figure 5 B2)	Subtidal, offshore, anoxic water conditions, below the SWB
LF10: Carbonate /quartz nodule rich black mudrock	Black, partially continuous parallel planar. Cherts and nodules highly developed (Figure 5 C1)	Calcite (45.92±10.74%), quartz (43.38±12.72%), muscovite (5.96±3.79%), ankerite (1.44±0.98%), halite (1.26±0.85%) and other minerals (pyrite, gypsum etc.)	Relatively high planktonic foraminifera content, crinoid fragments present (Figure 5 C2)	Subtidal, offshore, anoxic water conditions, below the SWB

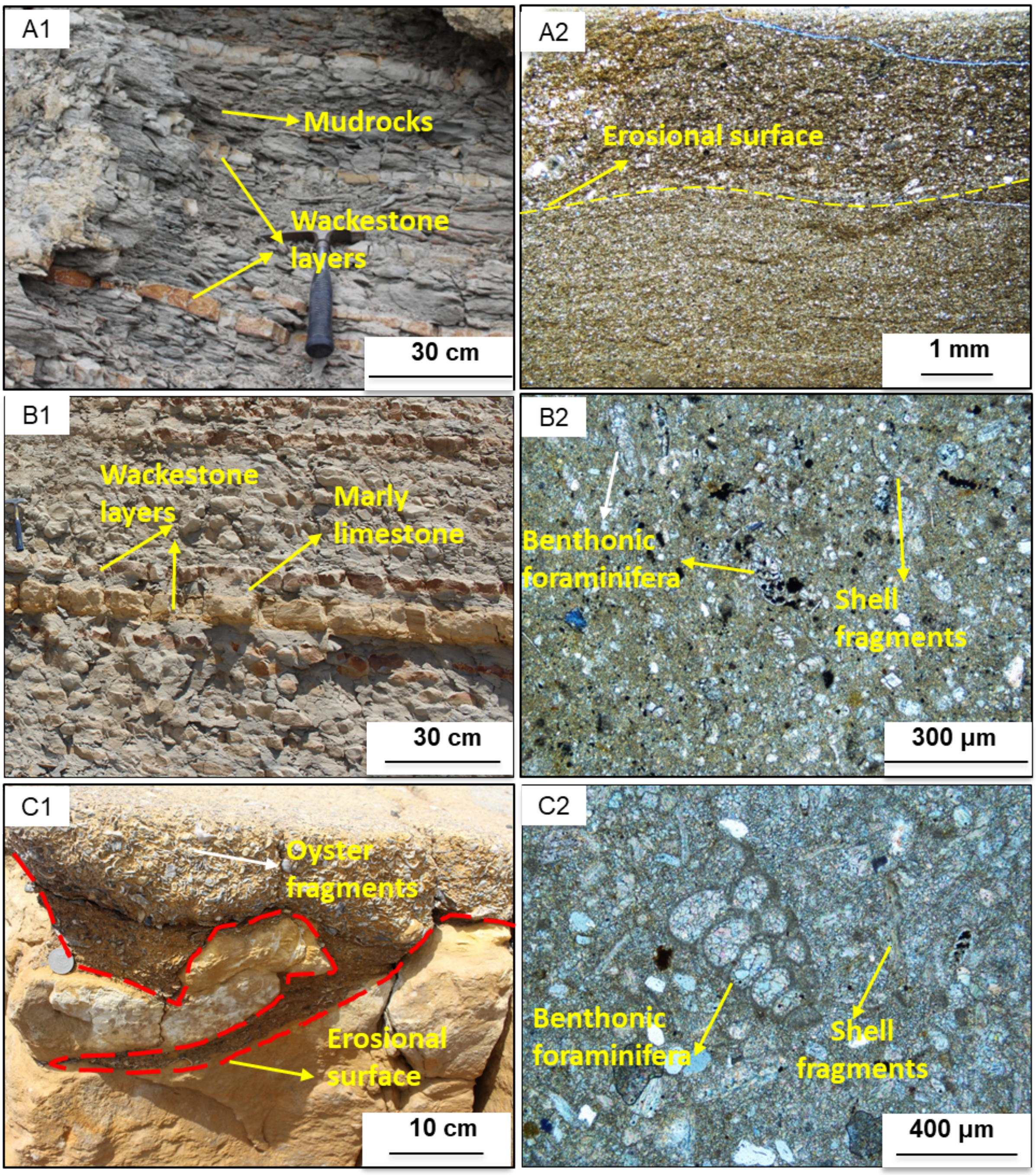

Figure 3 Summary of the Lithofacies 1-3 in the Azazoul section

LF1: (A1) Black mudrocks intercalated with some thinly limestone layers; (A2) Photomicrograph, illustrating the individual beds with an erosional surface at the bottom, each bed shows a normal grading texture; LF2: (B1) Illustrating the stacking patterns from wackestone to marly limestone; (B2) Photomicrograph, illustrating the microfossils components, including bivalve fragments, planktonic foraminifera and benthonic foraminifera; LF3: (C1) Outcrop photograph, illustrating the irregular and erosional karst contact between the *R.cushmani* zone and *W.archaeocretacea* zone; (C2) Photomicrograph, illustrating the microfossils components, including bivalve fragments and benthonic foraminifera

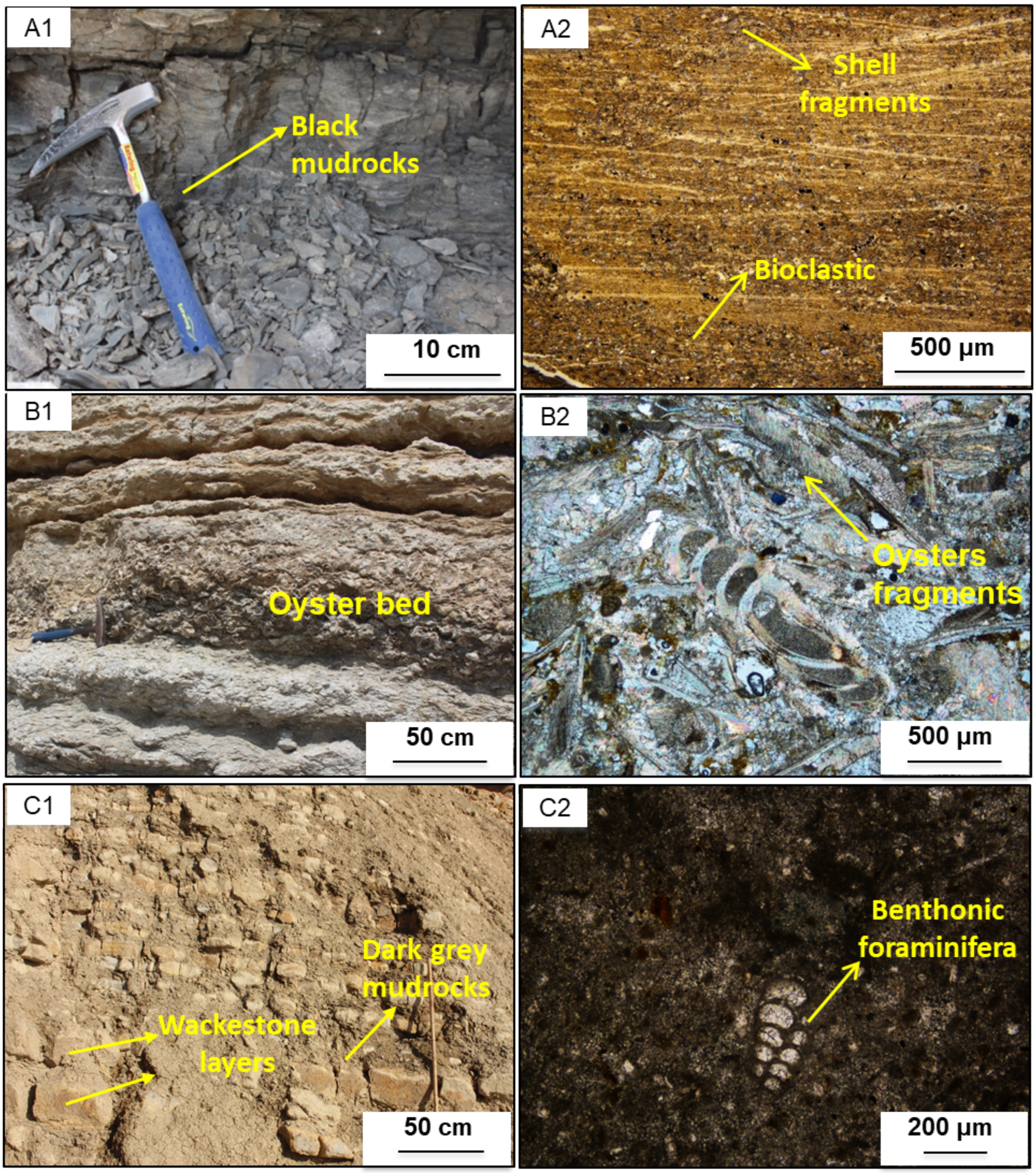

Figure 4 Summary of the lithofacies 4 to lithofacies 7 in the Azazoul section

LF4: (A1) Black mudstone bed with a thickness of 80 cm; (A2) Photomicrograph, illustrating silt-bearing and clay-rich mudstone. LF5 and LF6: (B1) Illustrating grainstone-floatstone beds (LF5); (B2) Photomicrograph showing benthonic foraminifera, echinoid, and oyster fragments in a grainstone-floatstone bed; LF7: (C1) Grey nodular limestone interbedded with dark grey mudstone, individually bed rare thicker than 20cm; (C2) Photomicrograph, illustrating a wackestone texture with some bivalve fragments and foraminifera.

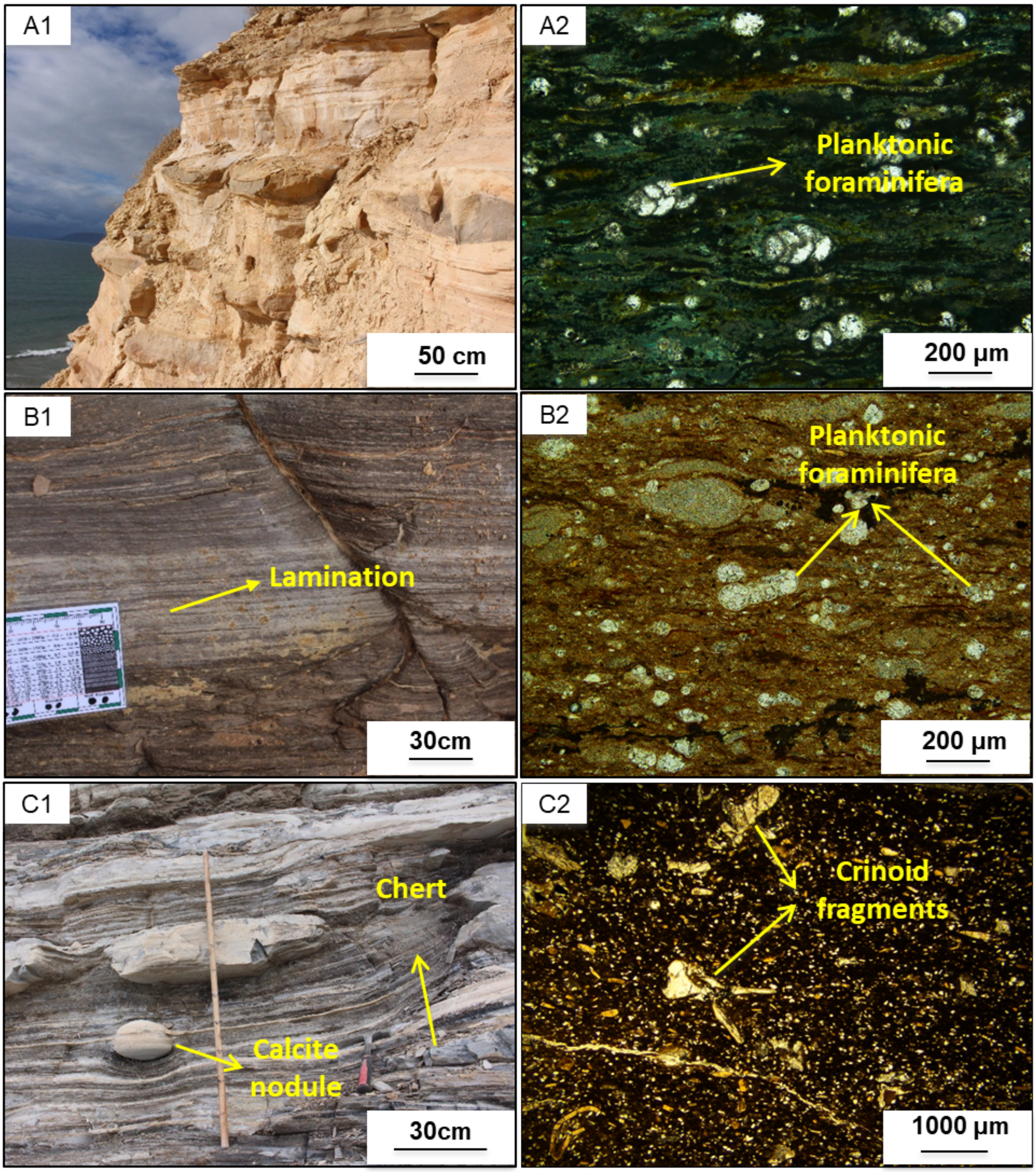

Figure 5 Summary of the lithofacies 6-9 in the Azazoul section

LF8: (A1) Large calcite nodules intercalated within the yellowish and reddish fine-grain limestone-marly limestone layers; (A2) Photomicrograph, showing the presence of abundant planktonic foraminifera and some shell fragments; LF 9: (B1) Partially laminated calcite-rich black mudstone; (B2) Photomicrograph, planktonic foraminifera highly developed in the OM-rich mudstone. LF10: (C1) Abundant nodules within quartz-rich black mudstone; (C2) Photomicrograph, showing the presence of crinoids and planktonic foraminifera in the OM-rich black mudstone.

4.2. Bulk carbonate $\delta^{13}C$ and $\delta^{18}O$

The $\delta^{13}C$ value at the base of the *R. cushmani* zone is +1.74‰ increasing upward gradually to +3.14‰ towards the middle part of this stage. Subsequently, there is a decrease to +1.54‰ (Figure 2) (Table 2). Moving into the lower *W. archaeocretacea* zone, the $\delta^{13}C$ values initially decrease to +1.30‰, and subsequently most values present a continuous value around +2‰. The middle *W. archaeocretacea* zone is characterised by the highest $\delta^{13}C$ values, with an average value of +3.45‰, peaking at +3.93‰. Thereafter, $\delta^{13}C$ values drop dramatically, reaching a minimum value of -3.50 ‰ at the top of *W. archaeocretacea* zone. The $\delta^{13}C$ values in the *H. helvetica* zone oscillate between -2.38 ‰ and -2.54‰.

The oxygen isotope values in the Azazoul section exhibit different relationships with the carbon isotope values in different zones. The oxygen isotope values show a negative relationship to the carbon isotope values in the middle *W. archaeocretacea* zone and upper *H. helvetica* zone, while showing a positive relationship in the *R.cushmani* zone, lower *W. archaeocretacea* zone and lower *H. helvetica* zone. A cross-plot of $\delta^{13}C$ and $\delta^{18}O$ values illustrates that most of the data are distributed within an $\delta^{18}O$ range from -3.5 ‰ to -1.0 and $\delta^{13}C$ range from -1‰ to +4‰ (Figure 6). The outlier-circled points with negative $\delta^{13}C$ values are predominantly from the *H. helvetica* zone (Figure 2) and are interpreted to reflect diagenetic alternation.

Table 2 Summary of the $\delta^{13}C$ and $\delta^{18}O$ values in the three zones of the Azazoul section

Isotope	Planktonic foraminifera zones	n	Mean (10^{-3})	Min (10^{-3})	Max (10^{-3})	SD (10^{-3})
$\delta^{13}C_{VPDB}$	*H.helvetica*	37	0.28	-2.38	2.54	1.08
	W.archaeocretacea	51	1.79	-3.5	3.93	1.24
	R.cushmani	18	2.44	1.54	3.24	0.52
$\delta^{18}O_{VPDB}$	*H.helvetica*	37	-2.80	-3.29	-1.91	0.34
	W.archaeocretacea	51	-1.85	-3.14	0.75	0.41
	R.cushmani	18	-1.61	-2.21	-1.15	0.24

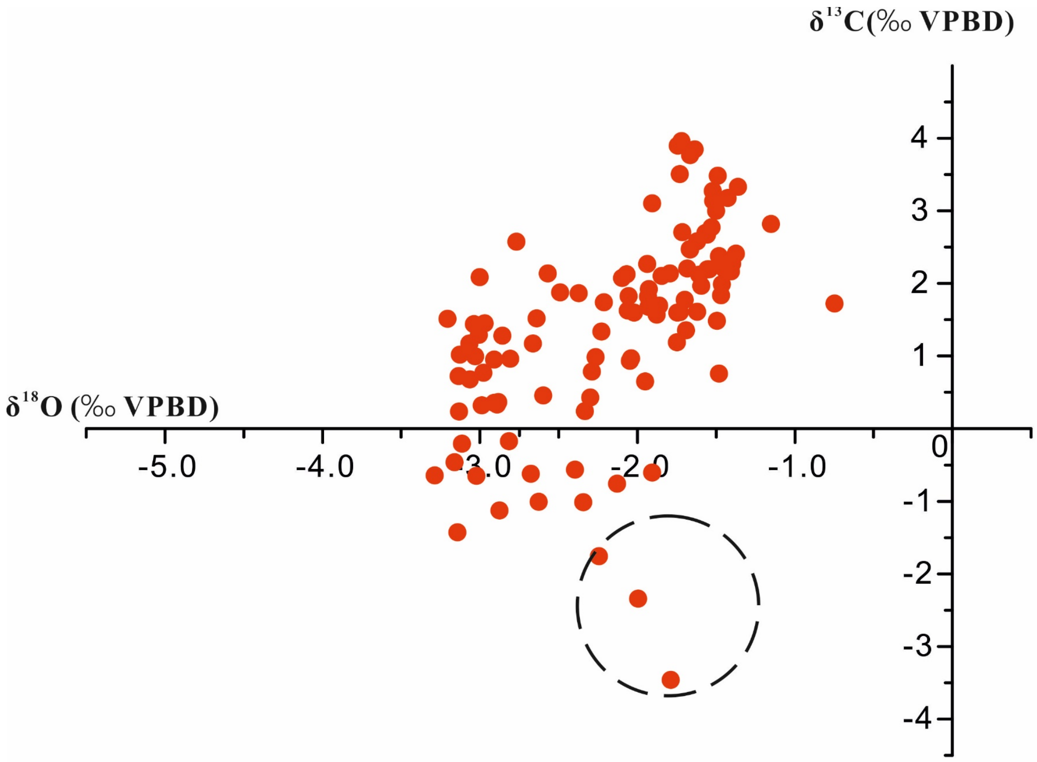

Figure 6 δ. ^{13}C and δ^{18}O crossplot illustrating the correlations between carbon and oxygen isotope data in the Azazoul section

4.3. Trace and Major Elements

Trace and major elements were analysed (Figure 7 and Table 3), with the purpose to explore the palaeoenvironment changes controlling the distribution of different lithofacies spatially and temporally.

4.3.1. Detrital influx sensitive elements

The concentrations of aluminium (Al), titanium (Ti), thallium (Th), and zirconium (Zr) show extremely strong correlation with each other in the Azazoul section (Figure 7), particularly evident in the ratios Al/Ti (R^2=0.97) and Al/Zr (R^2=0.96). The high concentrations of these elements in certain intervals of the *R. cushmani* and *W. archaeocretacea* zone are associated with abundant clay mineral content of LF1 and LF4. This suggests a significant terrigenous input, leading to the deposition of clay-rich mudstones in these intervals. All the other lithofacies developed in the *R. cushmani* and the *W. archaeocretacea* zones show minor concentrations of these elements. These suggests that these lithofacies experienced relatively lower terrigenous input. Low concentrations of these elements in the *H. helvetica* zone are consistent with the lower proportion of clay mineral content in LF8, L9, and LF10, indicating lower detrital influx during the deposition of organic-rich mudstone in this zone.

Table 3 Summary of major and trace elements in the Agadir Basin

Elements	Planktonic foraminifera zones	n	Min	Max	Mean	SD	Element/Al_{As} Wedepohl(1971)
Al (%)	*H.helvetica*	13	0.33	4.11	1.54	0.98	8.84
	W.archaeocretacea	15	0.46	11.4	5.52	4.01	
	R.cushmani	10	0.34	7.37	3.12	2.28	
Ti/Al (10^{-4})	*H.helvetica*	13	395	627	519	65.0	520
	W.archaeocretacea	15	442	805	616	97.0	
	R.cushmani	10	608	818	713	72	
Zr/Al (10^{-4})	*H.helvetica*	13	1.21	25.4	15	6.39	18.1
	W.archaeocretacea	15	0	22.0	14.0	6.90	
	R.cushmani	10	15.4	21.1	18.5	1.64	
Th/Al (10^{-4})	*H.helvetica*	13	0	3.33	1.70	0.79	1.36
	W.archaeocretacea	15	0.75	6.07	1.88	1.52	
	R.cushmani	10	0.96	6.95	2.79	2.32	
P/Al (10^{-4})	*H.helvetica*	13	347	4790	1886	1082	79
	W.archaeocretacea	15	41.3	502	163	121	
	R.cushmani	10	79.4	432	201	120	
Ni/Al ($10^{-4)}$	*H.helvetica*	13	9.04	82.4	43.0	22.0	7.69
	W.archaeocretacea	15	2.23	7.37	3.72	1.25	
	R.cushmani	10	2.53	4.72	3.75	0.59	
Zn/Al (10^{-4})	*H.helvetica*	13	3.46	449	151	138	10.7
	W.archaeocretacea	15	3.05	64	10.2	15	
	R.cushmani	10	4.72	23.5	7.54	5.46	
Cu/Al (10^{-4})	*H.helvetica*	13	4.14	37.4	18.8	10.70	5.09
	W.archaeocretacea	15	0	7.59	1.61	2.01	
	R.cushmani	10	0.81	2.53	1.30	0.57	
V/Al (10^{-4})	*H.helvetica*	13	32.6	730	200	185	14.7
	W.archaeocretacea	15	4.8	19.8	10.1	5.73	
	R.cushmani	10	1.07	16.7	8.86	5.73	
Mo/Al (10^{-4})	*H.helvetica*	13	1.72	15.3	8.41	4.03	2.9
	W.archaeocretacea	15	0.05	1.08	0.34	0.31	
	R.cushmani	10	0.11	1.34	0.45	0.39	
U/Al (10^{-4})	*H.helvetica*	13	1.83	24.3	10.4	6.75	0.42
	W.archaeocretacea	15	0.46	10.8	3.69	4.22	
	R.cushmani	10	0.81	16.0	4.82	5.09	

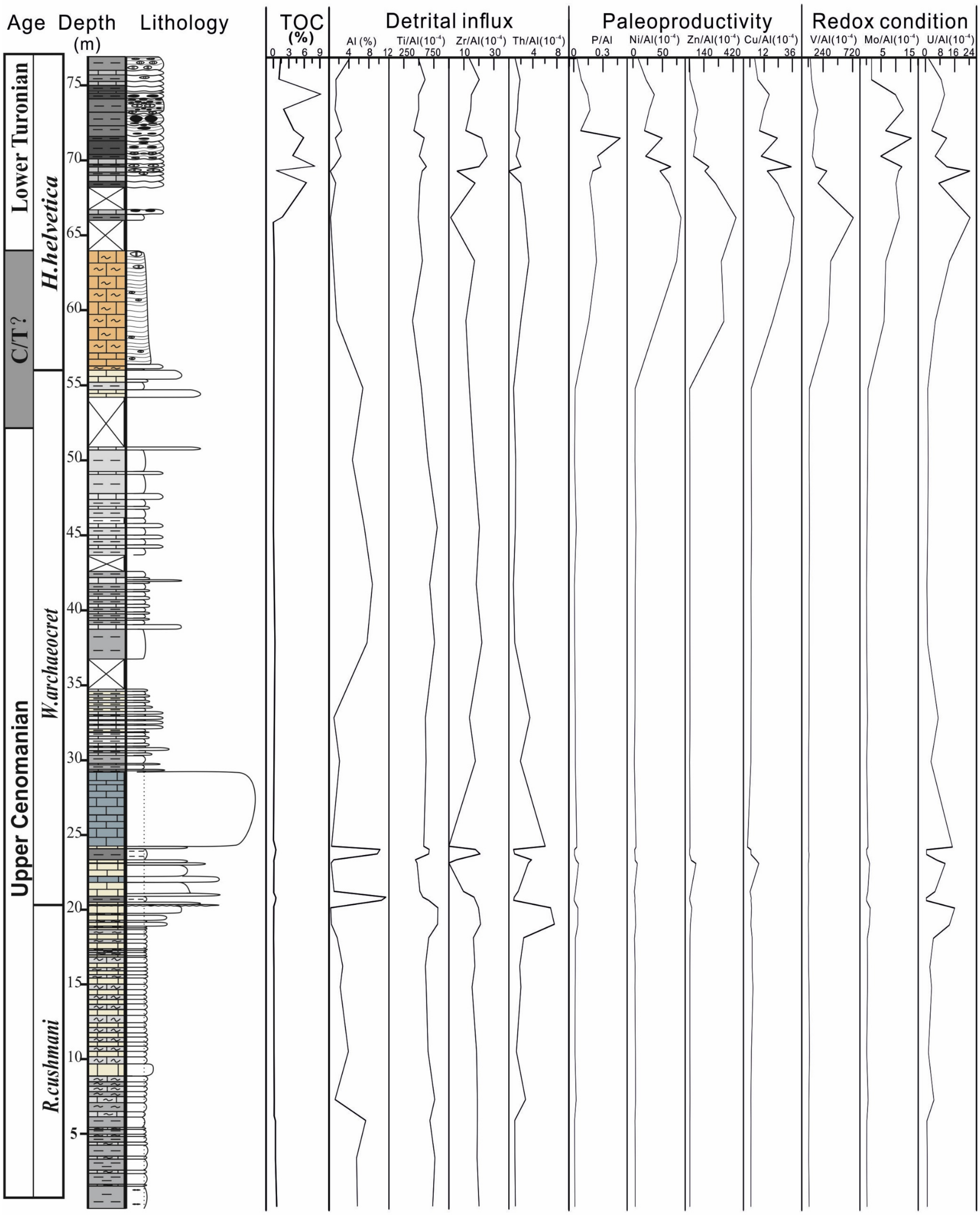

Figure 7 Enrichment factors for proxies representing the clastic influx, redox and palaeoproductivity, as well as TOC values in the Azazoul section

4.3.2. Palaeoproductivity-sensitive elements

Owing to the high detrital influx, it is possible to use the ratio of elements / Al to correct the possible dilution by organic matter and authigenic minerals (Calvert and Pedersen, 1993; Morford and Emerson, 1999), presenting results as Al-normalized elements values (Figure 7 and Table 3). These elemental concentrations are based on the comparison of element/Al ratios to those in a standard shale (Turekian and Wedepohl, 1961; Wedepohl, 1971; Calvert and Pedersen, 1993; Wedepohl, 1995; Morford and Emerson, 1999; Van der Weijden, 2002).

Phosphorus (P), nickel (Ni), zinc (Zn), and copper (Cu), can act as micronutrients that are commonly found in high concentration, fixed in sediments associated with organic matter preservation in the sediments (Tribovillard et al., 2006). Thus, these elements can be reliable indicators of OM productivity. Most of these Al-normalized elements show comparable trends, with moderate to high correlations with each other ($0.18<R^2>0.90$) (Figure 7 and Table 3).

These elements show a depleted concentrations in the *R. cushmani* and *W. archaeocretacea* zone, indicating a relatively lower level of productivity. However, throughout the *H. helvetica* zone, there is a moderate to significant enrichment in the concentration of these elements, suggesting moderate levels of productivity during this interval in the Agadir Basin.

4.3.3. Redox conditions sensitive elements

The Al normalized redox-sensitive elements, such as Vanadium, Molybdenum and Uranium, exhibit a similar trend to the productivity-sensitive elements in the Azazoul section(Figure 7 and Table 3). These elements also present depleted concentrations in the basal beds of this section, followed by a significant increase in concentration in the upper beds.

These redox-sensitive elements display extremely low concentrations in the *R. cushmani* and *W. archaeocretacea* zones, indicating prevailing oxygenated water conditions in these intervals. These elements are significantly to extremely concentrated in most intervals of the *H. Helvetica* zone, although a few intervals are associated with moderate concentration. The high concentrations provide strong evidence for the presence of anoxic bottom water during the deposition of organic-rich mudstones.

4.4. Total organic carbon and Rock-eval

The TOC content in the sediments of the *R. cushmani* and *W. archaeocretacea* zones is relatively low, even in the black mudstones developed in LF1 and LF4, with TOC values ranging from 0.4% to 0.6% (Figure 7). These mudstones are in an immature to early mature stage with the Tmax values ranging from 412 to 423 ℃. Hydrogen Index (HI) values for these sediments are between 30 and 136 mg HC/g TOC, and the Oxygen Index (OI) values range from 88 to 100 mg CO2/g TOC. The dominant kerogen of organic matter in the sediments is Type III with minor Type II.

Lithofacies LF9 and LF10 in the upper *H. helvetica* interval are characterised by high TOC contents. The sediments with a total thickness of approximately 10 metres have an average TOC value of 2.5 wt.%. The maximum TOC value of 9.2 wt.% is recorded in upper part of this interval. The Hydrogen Index (HI) values for these sediments range from 540 to 980 mg HC/g TOC, while the Oxygen Index (OI) values in this interval range from 39 to 1229 mg CO2/g TOC. The kerogen type of organic matter shows a mixture of type I and type II. The Tmax values of these black shales are relatively low from 410 ℃ to 414 ℃, showing an immature stage.

5. Discussion

5.1. Cenomanian/Turonian Stratigraphic Framework

The lack of datable in the Agadir Basin has resulted in poor biostratigraphic resolution, making it challenging to establish a reliable C/T stratigraphy in the region. This limitation has hindered the discrimination between global and local influences on palaeoenvironmental perturbations in this basin. However, the $\delta^{13}C$ signature of the marine carbonates provides a powerful and complementary tool for C/T boundary identification, allowing regional and global correlation despite the biostratigraphic uncertainties (Keller et al., 2001; Keller et al., 2004; Tsikos et al., 2004; Caron et al., 2006; Jarvis et al., 2011; Farouk et al., 2017; Falzoni et al., 2018; Abdelhady et al., 2021; Salhi et al., 2022). However, an uncertainty that needs to be considered and mitigated, is that $\delta^{13}C$ signature is readily modified by interaction with diagenetic fluids. The cross-plot of $\delta^{13}C$ and $\delta^{18}O$ values (Figure 6) shows a dominantly positive correlation, indicating some influence of diagenesis on $\delta^{13}C$ values. However, despite this diagenetic influence, most of the $\delta^{13}C$ values track published global changes well, exhibiting the characteristic positive excursion associated with enhanced organic matter preservation during the OAE2 and negative $\delta^{13}C$ excursion after the OAE2 interval (Figure 8) (Keller et al., 2004; Tsikos et al., 2004; Jarvis et al., 2011; Farouk et al., 2017; Kuhnt et al., 2017; Abdelhady et al., 2021; Salhi et al., 2022). Therefore, despite the potential diagenetic influence, these $\delta^{13}C$ values in this study are likely to be close to the primary isotopic composition and can be reliably applied for regional and global correlation.

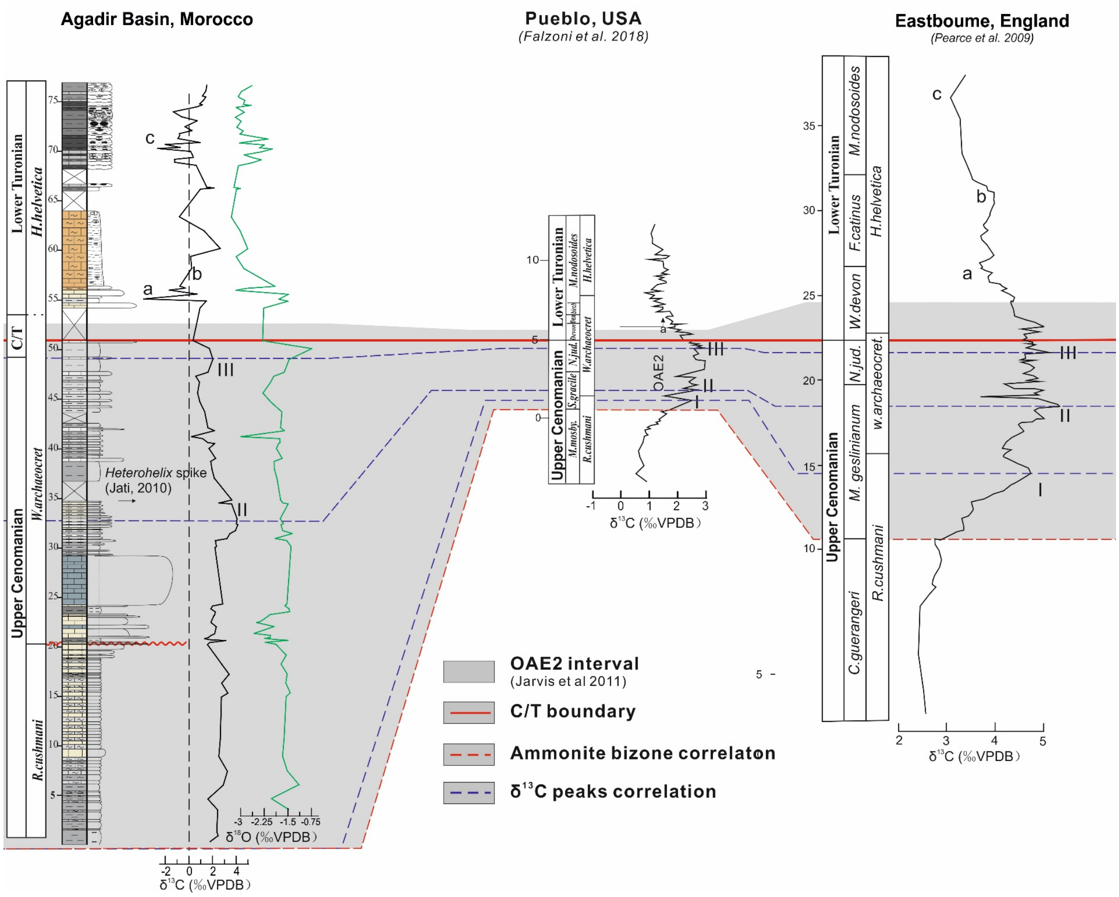

Figure 8 Carbon isotope curves correlation of the Azazoul section (Morocco), Eastbourne section (UK) and Pueblo section (USA)

Three distinct peaks have been commonly identified in the C/T $\delta^{13}C$ profiles, and are referred as A, B and C (Pearce et al., 2009; Jarvis et al., 2011) or I, II, III (Caron et al., 2006). Using the biostratigraphic framework presented in this study as an age control, enabling to recognise several related $\delta^{13}C$ peaks during the C/T interval (Figure 8). Due to the absence of ammonites in the Agadir Basin, which are typically used as the definitive age dating standard, the identification C/T boundary in this study is based on $\delta^{13}C$ correlation with the published planktonic foraminifera zones provided by Jati et al., 2010.

The last occurrence of the *R. cushmani* was identified just below the erosional karst surface (Gertsch et al., 2010a; Jati et al., 2010), and no *R. cushmani* species was found in the overlying beds. Peak I of $\delta^{13}C$ curves is missing in the studied upper *R. cushmani* interval. Based on the $\delta^{13}C$ profiles in the lower *R. cushmani* zone studied by Gertsch et al. (2010) and

Jati et al. (2010), an initial rapid increase in $\delta^{13}C$ values was recognised in the *R. cushmani* interval. This suggests that Peak I might be absent in the studied interval, and the entire studied *R. cushmani* interval can be placed within the OAE2 interval. Jati et al (2010) recognised the presence of heterohelix spike around this $\delta^{13}C$ peak, which is a common feature observed above Peak II in the Eastbourne and Pueblo sections (Keller et al., 2004; Tsikos et al., 2004; Caron et al., 2006; Keller, 2008; Keller et al., 2008). This suggests the maximum $\delta^{13}C$ peak in the Azazoul section is likely to be coeval with Peak II (Figure 8).

The first occurrence of *Helvetoglobotruncana helvetica* in the Azazoul section was recognised by Jati et al (2010) at the bottom of yellowish-reddish limestone beds (at 55m), below which is an erosional surface filled with bioclastic conglomerates. In spite of the possibility of a diachronous planktonic foraminiferal zone, Peak Ш is typically identified below the first occurrence of *H. helvetica*. In this case, the only salient peak between Peak II and the base of *H. helvetica* zone could be Peak III, if there is no significant hiatus present, and we tentatively place the C/T boundary above the Peak III based on correlation with the Eastbourne and Pueblo section (Figure 8).

Previous studies suggest the onset of the OAE2 interval commonly starts in the *M. geslinianum*/*S.gracile* zone, characterized as a sharp increase in $\delta^{13}C$ excursion, and ends above the C/T boundary in the *W.devonense* zone, with a decrease in $\delta^{13}C$ values (Jarvis et al., 2011). Therefore, the OAE2 interval in the Agadir Basin is identified from the upper part of the Late Cenomanian to very lower part of the Early Turonian (Figure 8).

5.2. Palaeoenvironments and sea level changes

The integration of trace elements data and lithofacies, including lithological changes, mineral compositions, and the presence of fossil assemblages, is crucial for understanding and identifying palaeoenvironmental conditions and evolution in the Agadir Basin. The detrital input and fluctuation of bottom water oxygen concentration from the Late Cenomanian to Early Turonian interval are analysed to assess the influences of the OAE2 and marine transgression on the C/T sediments in studied basin.

The U-EF vs. Mo-EF graph (Figure 9), based on multi-parameter datasets, has been demonstrated to be a reliable tool for palaeoredox condition analysis in various palaeoceanographic systems (Algeo and Tribovillard, 2009; Tribovillard et al., 2012). It can also be used to in interpret the degree of water mass restriction (Figure 9). Both U and Mo show minor enrichment in oxic water conditions and moderate enrichment (EFs<10) in dysoxic water conditions, while anoxic/euxinic water conditions yield high enrichment (EFs>10) (Tribovillard et al., 2012). Tribovillard et al., (2012) defined the following relationship: Low Mo/U ratios (~0.3×SW) in unrestricted marine systems; Intermediate Mo/U ratios (~1×SW) in suboxic and anoxic conditions; High Mo/U ratios (~3×SW) in strongly euxinic water conditions. However, it's important to note that these parameters are derived from present-day marine water values and are most suitable for unrestricted environments (Tribovillard et al., 2012).

Based this data and interpretations provided, the Late Cenomanian and the Early Turonian interval in the Azazoul section can be characterised as having mixed anoxic/dysoxic/oxic water conditions. The U-EF vs. Mo-EF graph indicates that there was intermittent presence of anoxic water conditions in the Late Cenomanian interval, but these conditions became more common in the Early Turonian interval, indicating a shift towards more reducing conditions (Figure 10). These results are consistent with the Ni/Co-U/Th cross plot (Jones and Manning, 1994). Furthermore, the Mo-U covariation analysis suggests the Agadir Basin experienced open marine conditions throughout the C/T interval, in accordance with the other trace elements concentrations.

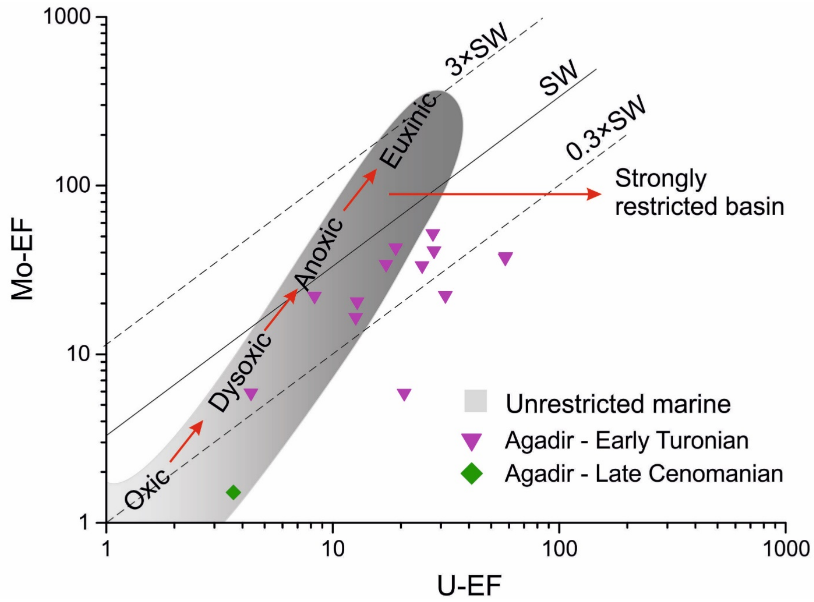

Figure 9 U–EF vs. Mo–EF for the C/T sediments in the Agadir Basin (Algeo and Tribovillard, 2009; Tribovillard et al., 2012).

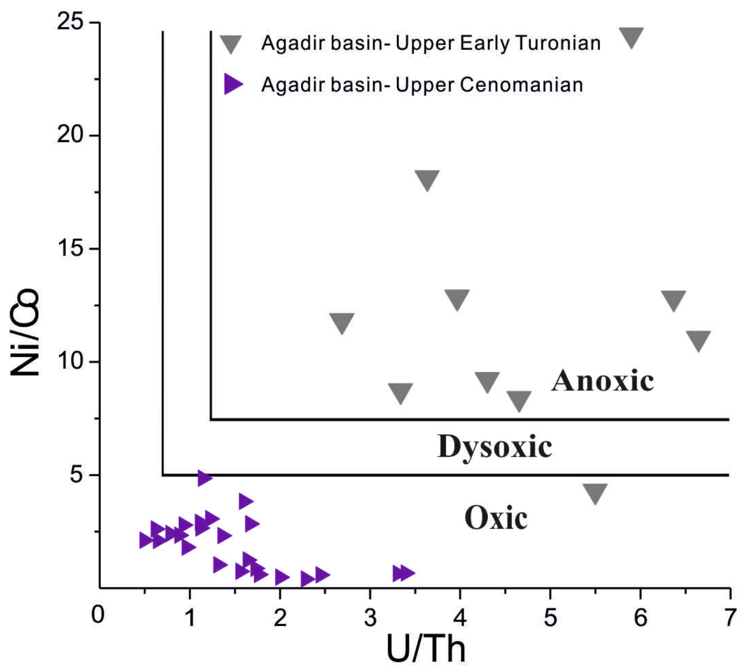

Figure 10 Cross-plot of TE ratios as palaeoredox proxies in the Agadir Basin, based on Jones and Manning (1994) and Hatch and Leventhal (1992).

5.2.1. *R. cushmani* zone

The data and interpretations provided in the study suggest that sediments in the *R. cushmani* zone of the Agadir Basin were deposited during the OAE2 interval. The absence of OM-rich black mudstone deposition supports inference of dominantly shallow water oxic conditions during this time. This is further evidenced by the low concentration of redox-sensitive elements in the sediments (Figure 7). The high detrital influx indicated by high Al concentration (>10 wt. %) suggests increased weathering during the Late Cenomanian, likely related to global warming (Leckie et al., 2002; Kidder and Worsley, 2010; Jarvis et al., 2011). The presence of high clay mineral content in the organic-poor mudstones (LF1, Table 1) at the base of studied *R.cushmani* zone supports the inference of a humid climate during this interval(Chamley, 1989; Bolle and Adatte, 2001), favouring for the significant weathering.

is consistent with the increased weathering owing to the global warming during the Late Cenomanian. The overlying fine-grain limestone/marly limestone couplet has low detrital sensitive element concentrations and rare clay mineral content, suggesting a significantly decreased terrigenous input.

The lack of significant change in sea-level or bottom water conditions, as indicated by the faunal assemblages (which suggests a range between the FWWB and SWB) (Figure 10), suggests the decreased clastic input in this interval is related to decreased weathering rather than rapid marine transgression. A cooling period associated with decreased weathering and re-oxygenation of sediments was recognised in the Eastbourne and Pont D'Issole C/T sections, during the uppermost *R.cushmani* interval (Figure 11) (Jarvis et al., 2011), which is consistent with the findings in this study.

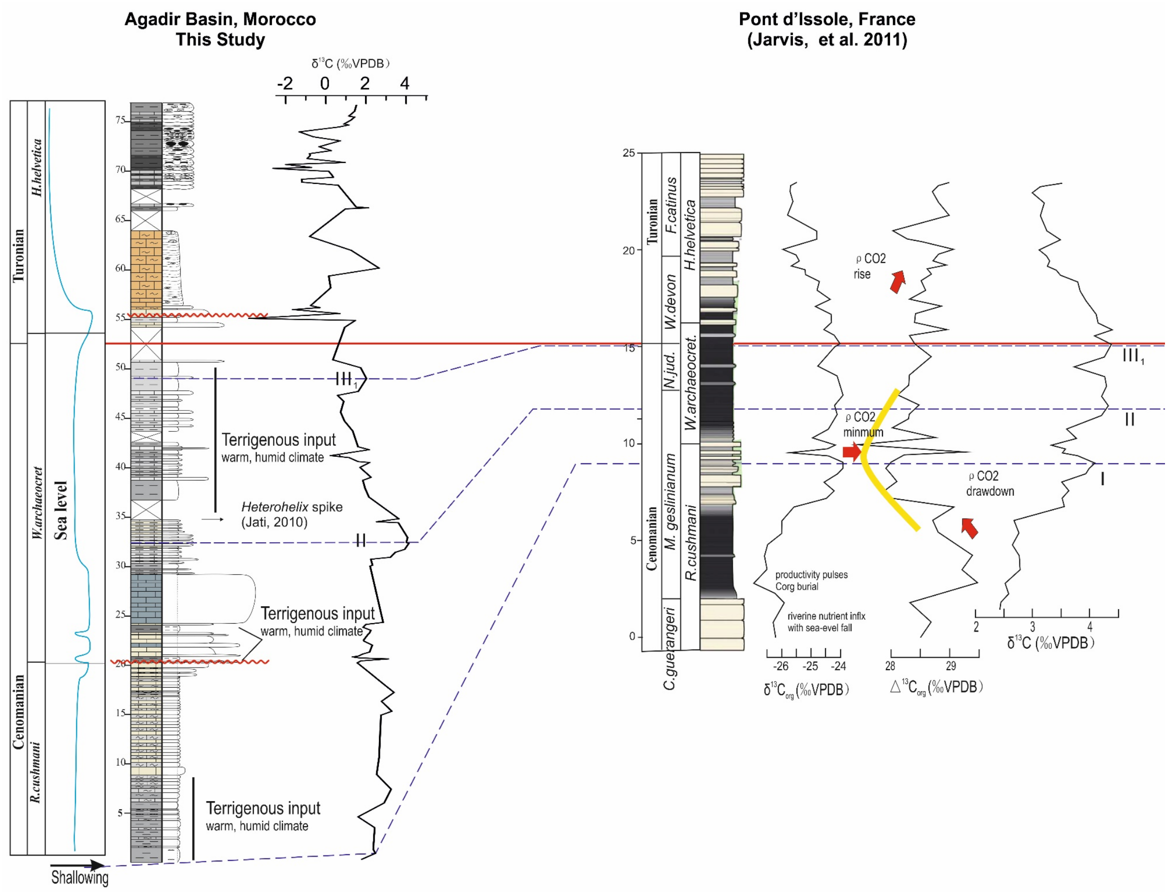

Figure 11 Correlation of the sections in this study with Pont D'Issole sections based on carbon isotope curves and biostratigraphy, to show the ρCO2 perturbation across the OAE2 interval globally.

5.2.2. *W. archaeocretacea* zone

The extremely high detrital influx, indicated by high Al concentration (Al_2O_3 up to 21 wt. %) (Figure 7) and kaolinite content (>30%) (Table 1), suggests a significant continental weathering occurred during *W. archaeocretacea* zone(Fedo et al., 1995; Liu et al., 2020). this is in accordance with the significantly increased pCO2 readings globally after the 'Plenus Cold Event' (Jarvis et al., 2011) (Figure 11). Dominantly oxic water conditions are indicated by depleted concentration of redox-sensitive elements (Figure 7 and Figure 10) throughout the *W. archaeocretacea* interval. These conditions are unfavourable for the organic matter preservation (rarely higher than 0.5%) in this interval. These clay-rich but organic-poor mudstones are likely driven by a combination of increased detrital input and higher sea levels.

5.2.3. *H. helvetica* zone

The deposition of a yellowish limestone (LF8) is interpreted to record a rapid sea level fall during the basal part of the *H. helvetica* zone. This is terminated by an erosional surface. Subsequently, the presence of OM-rich black mudstone lithofacies (LF9 and LF10) suggests a significant sea level transgression. Trace elemental analysis further suggests predominantly anoxic water conditions during this interval, though with periods of oxic/dysoxic redox conditions intercalated occasionally (Figure 10).

To conclude, dominantly oxic water conditions during the Late Cenomanian interval, equivalent with OAE2 interval, are associated high terrigenous influence, reflecting a globally warming paleoclimate. The transition into the Early Turonian is marked by a short marine regression, followed by a major marine transgression, which can be correlated with the global eustatic cycle (Haq, 2014) (Figure 12).

The OM-rich black mudstone deposition is coeval with the global Early Turonian transgression (Friedrich et al., 2012; Jarvis et al., 2015) (Figure 12). The dramatic palaeoenvironment change that occurred in the Agadir Basin from the Late Cenomanian to Early Turonian might suggest the palaeoenvironment change was not soley related to the global marine transgression, but might have also involved tectonic subsidence (Jati et al., 2010).

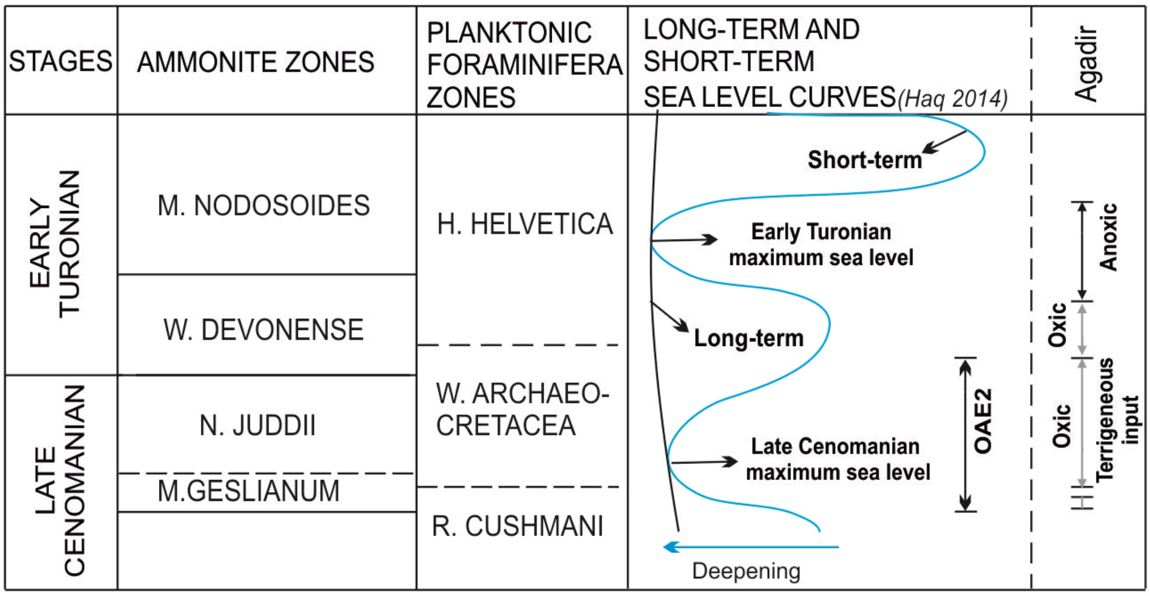

Figure 12 The position of OAE2 interval and black mudstones in global eustatic cycle.

5.3. Controls of organic matter accumulation

The absence of OM-rich mudstones during the Late Cenomanian interval, associated with the OAE2, can be attributed to several factors. The low organic content during the OAE2 interval is likely a result of low primary productivity, prevailing oxic conditions and strong dilution (Figure 7) owing to considerable terrigenous input. These factors together limited the OM accumulation and preservation. Some discrete intervals with low terrigenous input are still associated with low OM enrichment, suggesting that terrigenous dilution was not the only contributor to impede the organic matter preservation. In addition to terrigenous dilution, biogenic dilution is also a potential control for the OM-poor sediments (Tyson, 2001), particularly in shallow marine regimes like the Agadir Basin, where a strong dilution by non-hydrogen-rich biogenic components, such as shell fragments, could reduce overall TOC content. In these shallow marine environments with moderate to low primary production, strong biogenetic dilution, and poor preservation potential due to oxic bottom waters, organic carbon is less likely to accumulate.

The OM-rich black mudstones were developed in the Agadir Basin during the Early Turonian, which coincides with the global sea level maximum (Haq, 2014) (Figure 12). This is evident from the elevated concentrations of increase of OM productivity-sensitive (Ni, Zn and Cu) and redox-sensitive (Mo, V and U) element concentration during organic carbon deposition. The decrease in terrigenous input, indicated by low detrital-sensitive element concentrations, likely occurred as a result of rapid marine transgression due to sea level rise during the Turonian. Widespread anoxic conditions are indicated by high or extremely high redox-sensitive element concentration in the OM-rich black mudstones (Figure 7), but this anoxia was not consistent and was sporadically interrupted by oxic/dysoxic water conditions indicated by lower TE concentrations. The latter is also demonstrated by the presence of discrete horizons with bioturbation (Figure 5, B1). The correlation between organic matter enrichment and productivity is stronger than the correlation with oxygen deficiency, but the highest organic matter accumulation was not associated with the most reducing conditions or highest productivity (Figure 7). The decrease in organic matter content in the middle interval, corresponding to a high content of siliceous lithologies (chert dominant) (Figure 5, C1), suggests a high amount of biogenic material dilution occurred during this time.

The data suggests the highest OM concentrations in the Early Turonian interval were influenced by the combined action of relatively high productivity, low biogenic dilution, optimum preservation conditions during periods of oxygen deficiency and low detrital influx.

6. Conclusions

The location of the OAE2 and Cenomanian-Turonian boundary in the Agadir Basin is defined with greater precision, based on integration of previously published biostratigraphy (planktonic foraminifera) and new high-resolution $\delta^{13}C$ data.

A total of ten lithofacies are recognised in the Azazoul section. The Late Cenomanian sediments record shallow marine environments, with progressive deepening into the Early Turonian strata Lower Turonian, the latter of which is attributed to the Early Turonian global sea level rise.

No organic matter-rich black mudstone was recognised in the Azazoul section during the OAE2 interval. Several dark grey mudstone beds deposited during the OAE2, but these exhibit low OM enrichment, related to low productivity, oxidation of OM and high biogenic and clastic dilution. Overall, the environment of deposition at the time of OAE2 is interpreted to be an oxic shallow marine water condition.

OM-rich black mudstones are developed in post-OAE2 Early Turonian strata, which OM productivity-sensitive (Ni, Zn and Cu) and redox-sensitive (Mo, V and U) element concentration indicate were associated with increased surface water productivity and oxygen-depleted bottom water conditions. The main control is suggested to be the global Early Turonian marine transgression.

7. Acknowledgements

The authors gratefully acknowledge the sponsoring companies of North Africa Research Group (NARG) and L'Office National des Hydrocarbures et des Mines (ONHYM) for their financial and scientific support. We thank Dr. Aude Duval-Arnould from the University of Manchester for her help and support during the fieldwork, Dr. Alastair Bewsher and Dr. Paul Lythgoe from the University of Manchester for the XRF analysis, Mr. Steve Stockley from the University of Manchester for the powder samples preparation, Dr. Stephen Crowley from the University of Liverpool for the stable carbon and oxygen isotope analysis, and Dr. John Waters from the University of Manchester for the XRD training. We also appreciate the help from Professor Cathy Hollis from the University of Manchester and Professor Gregory Price from the University of Plymouth for their critical suggestions.

References

Abdelhady, A.A., Farouk, S., Ahmad, F., Elamri, Z., Al-Kahtany, K., 2021. Impact of the late Cenomanian sea-level rise on the south Tethyan coastal ecosystem in the Middle East (Jordan, Egypt, and Tunisia): A quantitative eco-biostratigraphy approach. Palaeogeography, Palaeoclimatology, Palaeoecology 574, 110446.

Algeo, T.J., Tribovillard, N., 2009. Environmental analysis of paleoceanographic systems based on molybdenum–uranium covariation. Chemical Geology 268, 211-225.

Arthur, M.A., Dean, W.E., Pratt, L.M., 1988. Geochemical and climatic effects of increased marine organic carbon burial at the Cenomanian/Turonian boundary. Nature 335, 714.

Behrens, M., Siehl, A., 1982. Sedimentation in the Atlas Gulf I: lower cretaceous clastics, Geology of the northwest African continental margin. Springer, pp. 427-438.

Bolle, M.-P., Adatte, T., 2001. Palaeocene-early Eocene climatic evolution in the Tethyan realm: clay mineral evidence. Clay minerals 36, 249-261.

Brumsack, H.-J., 1989. Geochemistry of recent TOC-rich sediments from the Gulf of California and the Black Sea. Geologische Rundschau 78, 851-882.

Calvert, S., Pedersen, T., 1993. Geochemistry of recent oxic and anoxic marine sediments: implications for the geological record. Marine Geology 113, 67-88.

Caron, M., Dall'Agnolo, S., Accarie, H., Barrera, E., Kauffman, E.G., Amédro, F., Robaszynski, F., 2006. High-resolution stratigraphy of the Cenomanian–Turonian boundary interval at Pueblo (USA) and wadi Bahloul (Tunisia): stable isotope and bio-events correlation. Geobios 39, 171-200.

Chamley, H., 1989. Clay sedimentology. Springer Science & Business Media.

Daoudi, L., Rocha, F., Ouajhain, B., Dinis, J., Chafiki, D., Callapez, P., 2008. Palaeoenvironmental significance of clay minerals in Upper Cenomanian–Turonian sediments of the western High Atlas Basin (Morocco). Clay Minerals 43, 615-630.

Duval-Arnould, A., Schröder, S., Charton, R., Joussiaume, R., Razin, P., Redfern, J., 2021. Early post-rift depositional systems of the Central Atlantic: Lower and Middle Jurassic of the Essaouira-Agadir Basin, Morocco. Journal of African Earth Sciences 178, 104164.

El-Sabbagh, A., Tantawy, A.A., Keller, G., Khozyem, H., Spangenberg, J., Adatte, T., Gertsch, B., 2011. Stratigraphy of the Cenomanian–Turonian Oceanic Anoxic Event OAE2 in shallow shelf sequences of NE Egypt. Cretaceous Research 32, 705-722.

Falzoni, F., Petrizzo, M.R., Caron, M., Leckie, R.M., Elderbak, K., 2018. Age and synchronicity of planktonic foraminiferal bioevents across the Cenomanian–Turonian boundary interval (Late Cretaceous). Newsletters on Stratigraphy 51, 343-380.

Farouk, S., Ahmad, F., Powell, J.H., 2017. Cenomanian–Turonian stable isotope signatures and depositional sequences in northeast Egypt and central Jordan. Journal of Asian Earth Sciences 134, 207-230.

Fedo, C.M., Wayne Nesbitt, H., Young, G.M., 1995. Unraveling the effects of potassium metasomatism in sedimentary rocks and paleosols, with implications for paleoweathering conditions and provenance. Geology 23, 921-924.

Fonseca, C., Mendonça Filho, J.G., Lézin, C., Duarte, L.V., 2020. Organic facies variability and paleoenvironmental changes on the Moroccan Atlantic coast across the Cenomanian—Turonian Oceanic Anoxic Event (OAE2). International Journal of Coal Geology 230, 103587.

Forster, A., Schouten, S., Moriya, K., Wilson, P.A., Sinninghe Damsté, J.S., 2007. Tropical warming and intermittent cooling during the Cenomanian/Turonian oceanic anoxic event 2: Sea surface temperature records from the equatorial Atlantic. Paleoceanography 22.

Friedrich, O., Norris, R.D., Erbacher, J., 2012. Evolution of middle to Late Cretaceous oceans—a 55 my record of Earth's temperature and carbon cycle. Geology 40, 107-110.

Gale, A.S., Kennedy, W.J., Voigt, S., Walaszczyk, I., 2005. Stratigraphy of the Upper Cenomanian–Lower Turonian Chalk succession at Eastbourne, Sussex, UK: ammonites, inoceramid bivalves and stable carbon isotopes. Cretaceous Research 26, 460-487.

Gertsch, B., Adatte, T., Keller, G., Tantawy, A.A.A., Berner, Z., Mort, H.P., Fleitmann, D., 2010a. Middle and late Cenomanian oceanic anoxic events in shallow and deeper shelf environments of western Morocco. Sedimentology 57, 1430-1462.

Gertsch, B., Keller, G., Adatte, T., Berner, Z., Kassab, A., Tantawy, A., El-Sabbagh, A., Stueben, D., 2010b. Cenomanian–Turonian transition in a shallow water sequence of the Sinai, Egypt. International Journal of Earth Sciences 99, 165-182.

Haq, B.U., 2014. Cretaceous eustasy revisited. Global and Planetary Change 113, 44-58.

Hollard, H., Choubert, G., Bronner, G., Marchand, J., Sougy, J., 1985. Carte géologique du Maroc, scale 1: 1,000,000. Serv. Carte géol. Maroc 260.

Jarvis, I., Lignum, J.S., Gröcke, D.R., Jenkyns, H.C., Pearce, M.A., 2011. Black shale deposition, atmospheric CO2 drawdown, and cooling during the Cenomanian-Turonian Oceanic Anoxic Event. Paleoceanography 26.

Jarvis, I., Trabucho-Alexandre, J., Gröcke, D.R., Uličný, D., Laurin, J., 2015. Intercontinental correlation of organic carbon and carbonate stable isotope records: evidence of climate and sea-level change during the Turonian (Cretaceous). The Depositional Record 1, 53-90.

Jati, M., Grosheny, D., Ferry, S., Masrour, M., Aoutem, M., Icame, N., Gauthier-Lafaye, F., Desmares, D., 2010. The Cenomanian–Turonian boundary event on the Moroccan Atlantic margin (Agadir basin): Stable isotope and sequence stratigraphy. Palaeogeography, Palaeoclimatology, Palaeoecology 296, 151-164.

Jenkyns, H., Gale, A.S., Corfield, R., 1994. Carbon-and oxygen-isotope stratigraphy of the English Chalk and Italian Scaglia and its palaeoclimatic significance. Geological Magazine 131, 1-34.

Jenkyns, H.C., 2003. Evidence for rapid climate change in the Mesozoic–Palaeogene greenhouse world. Philosophical Transactions of the Royal Society of London A: Mathematical, Physical and Engineering Sciences 361, 1885-1916.

Jenkyns, H.C., 2010. Geochemistry of oceanic anoxic events. Geochemistry, Geophysics, Geosystems 11.

Jones, B., Manning, D.A., 1994. Comparison of geochemical indices used for the interpretation of palaeoredox conditions in ancient mudstones. Chemical Geology 111, 111-129.

Joo, Y.J., Sageman, B.B., Hurtgen, M.T., 2020. Data-model comparison reveals key environmental changes leading to Cenomanian-Turonian Oceanic Anoxic Event 2. Earth-Science Reviews 203, 103123.

Keller, G., 2008. Cretaceous climate, volcanism, impacts, and biotic effects. Cretaceous Research 29, 754-771.

Keller, G., Adatte, T., Berner, Z., Chellai, E., Stueben, D., 2008. Oceanic events and biotic effects of the Cenomanian-Turonian anoxic event, Tarfaya Basin, Morocco. Cretaceous Research 29, 976-994.

Keller, G., Berner, Z., Adatte, T., Stueben, D., 2004. Cenomanian–Turonian and δ13C, and δ18O, sea level and salinity variations at Pueblo, Colorado. Palaeogeography, Palaeoclimatology, Palaeoecology 211, 19-43.

Keller, G., Han, Q., Adatte, T., Burns, S.J., 2001. Palaeoenvironment of the Cenomanian–Turonian transition at Eastbourne, England. Cretaceous Research 22, 391-422.

Kidder, D.L., Worsley, T.R., 2010. Phanerozoic large igneous provinces (LIPs), HEATT (haline euxinic acidic thermal transgression) episodes, and mass extinctions. Palaeogeography, Palaeoclimatology, Palaeoecology 295, 162-191.

Kuhnt, W., Holbourn, A.E., Beil, S., Aquit, M., Krawczyk, T., Flögel, S., Chellai, E.H., Jabour, H., 2017. Unraveling the onset of Cretaceous Oceanic Anoxic Event 2 in an extended sediment archive from the Tarfaya-Laayoune Basin, Morocco. Paleoceanography 32, 923-946.

Leckie, R.M., Bralower, T.J., Cashman, R., 2002. Oceanic anoxic events and plankton evolution: Biotic response to tectonic forcing during the mid-Cretaceous. Paleoceanography 17, 13-11-13-29.

Liu, B., Song, Y., Zhu, K., Su, P., Ye, X., Zhao, W., 2020. Mineralogy and element geochemistry of salinized lacustrine organic-rich shale in the Middle Permian Santanghu Basin: Implications for paleoenvironment, provenance, tectonic setting and shale oil potential. Marine and Petroleum Geology 120, 104569.

Morford, J.L., Emerson, S., 1999. The geochemistry of redox sensitive trace metals in sediments. Geochimica et Cosmochimica Acta 63, 1735-1750.

Nouidar, M., 2002. Facies and sequence stratigraphy of a Late Barremian wave-dominated deltaic deposit, Agadir Basin, Morocco. Sedimentary Geology 150, 375-384.

Pearce, M.A., Jarvis, I., Tocher, B.A., 2009. The Cenomanian–Turonian boundary event, OAE2 and palaeoenvironmental change in epicontinental seas: new insights from the dinocyst and geochemical records. Palaeogeography, Palaeoclimatology, Palaeoecology 280, 207-234.

Salhi, I., Elamri, Z., Bazeen, Y.S., Ahmad, F., Mahmoudi, S., Farouk, S., 2022. Planktonic foraminifera and stable isotopes of the upper Cenomanian–middle Turonian in central Tunisia: Implications for bioevents synchronicity and paleoenvironmental turnover. Cretaceous Research 138, 105291.

Sames, B., Wagreich, M., Wendler, J., Haq, B., Conrad, C., Melinte-Dobrinescu, M., Hu, X., Wendler, I., Wolfgring, E., Yilmaz, I., 2016. Short-term sea-level changes in a greenhouse world—A view from the Cretaceous. Palaeogeography, Palaeoclimatology, Palaeoecology 441, 393-411.

Schlanger, S., Arthur, M., Jenkyns, H., Scholle, P., 1987. The Cenomanian-Turonian Oceanic Anoxic Event, I. Stratigraphy and distribution of organic carbon-rich beds and the marine δ13C excursion. Geological Society, London, Special Publications 26, 371-399.

Schlanger, S.O., Jenkyns, H., 1976. Cretaceous oceanic anoxic events: causes and consequences. Geologie en mijnbouw 55, 179-184.

Stets, J., Wurster, P., 1982. Atlas and Atlantic—structural relations, Geology of the Northwest African continental margin. Springer, pp. 69-85.

Tribovillard, N., Algeo, T., Baudin, F., Riboulleau, A., 2012. Analysis of marine environmental conditions based onmolybdenum–uranium covariation—Applications to Mesozoic paleoceanography. Chemical Geology 324, 46-58.

Tribovillard, N., Algeo, T.J., Lyons, T., Riboulleau, A., 2006. Trace metals as paleoredox and paleoproductivity proxies: an update. Chemical geology 232, 12-32.

Tsikos, H., Jenkyns, H., Walsworth-Bell, B., Petrizzo, M., Forster, A., Kolonic, S., Erba, E., Silva, I.P., Baas, M., Wagner, T., 2004. Carbon-isotope stratigraphy recorded by the Cenomanian–Turonian Oceanic Anoxic Event: correlation and implications based on three key localities. Journal of the Geological Society 161, 711-719.

Turekian, K.K., Wedepohl, K.H., 1961. Distribution of the elements in some major units of the earth's crust. Geological Society of America Bulletin 72, 175-192.

Tyson, R., 2001. Sedimentation rate, dilution, preservation and total organic carbon: some results of a modelling study. Organic Geochemistry 32, 333-339.

Van der Weijden, C.H., 2002. Pitfalls of normalization of marine geochemical data using a common divisor. Marine Geology 184, 167-187.

Wedepohl, K., 1971. Environmental influences on the chemical composition of shales and clays. Physics and Chemistry of the Earth 8, 307-333.

Wedepohl, K.H., 1995. The composition of the continental crust. Geochimica et cosmochimica Acta 59, 1217-1232.